Numerical Investigation of Configurations with Optimum Swirl Recovery for Propeller Propulsion Systems

Li, Qingxi; Liu, Xinyuan; Eitelberg, Georg; Veldhuis, Leo

DOI
10.2514/1.J057704

Publication date
2019

Document Version
Final published version

Published in
AIAA Journal: devoted to aerospace research and development

AIAA JOURNAL
Vol. 57, No. 4, April 2019

Numerical Investigation of Configurations with Optimum Swirl Recovery for Propeller Propulsion Systems

Qingxi Li,* Xinyuan Liu,† Georg Eitelberg,‡ and Leo Veldhuis§
Delft University of Technology, 2629 HS Delft, The Netherlands

DOI: 10.2514/1.J057704

This paper addresses the design of swirl recovery vanes for propeller propulsion in tractor configuration at cruise conditions using numerical tools. A multifidelity optimization framework is formulated for the design purpose, which exploits low-fidelity potential flow-based analysis results as input for high-fidelity Euler equation-based simulations. Furthermore, a model alignment procedure between low- and high-fidelity models is established based on a shape-preserving response prediction algorithm. Two cases of swirl recovery are examined. The first is the swirl recovery by the trailing wing, which leads to a reduction of the lift-induced drag. This is achieved by the optimization of the wing twist distribution. The second case is swirl recovery by a set of stationary vanes, which leads to production of additional thrust. In the latter case, four configurations are evaluated by locating the vanes at different azimuthal and axial positions relative to the wing. An optimum configuration is identified where the vanes are positioned on the blade-downgoing side downstream of the wing. For the configuration and conditions examined, the wing twist optimization reduces the induced drag by 3.9 counts (5.9% of wing-induced drag), whereas the optimized 4-bladed SRVs lead to an induced-drag reduction of 6.1 counts (9.2% of wing-induced drag).

Nomenclature

b	=	wing span, m
C_d	=	swirl recovery vane (SRV) sectional drag coefficient; $d/(0.5\rho V_\infty^2 c)$
$C_{D,i}$	=	induced drag coefficient; $D_i/(0.5\rho V_\infty^2 S)$
C_l	=	wing sectional lift coefficient; $l/(0.5\rho V_\infty^2 c)$
C_L	=	lift coefficient; $L/(0.5\rho V_\infty^2 S)$
C_p	=	pressure coefficient; $(p - p_\infty)/(0.5\rho V_\infty^2)$
C_T	=	thrust coefficient; $T/(\rho n_s^2 D^4)$
c	=	chord length, m
c_r	=	wing root chord length, m
D	=	propeller diameter, m
D_i	=	induced drag, N
$\boldsymbol{F}$	=	force vectors on wing panels, N
J	=	propeller advance ratio; $V_\infty/(n_s D)$
L	=	lift force, N
Ma_∞	=	freestream Mach number
N	=	blade count
$\boldsymbol{n}$	=	unit normal vector of wing panels
n_s	=	propeller rotation frequency, s^{-1}
R	=	propeller radius, m
r	=	radial coordinate, m
Δr	=	section span in SRV lifting line model, m
S	=	wing surface area, m^2
T	=	thrust force, N
$\boldsymbol{V}$	=	velocity vectors on wing panels, $m \cdot s^{-1}$
V_a, V_t	=	axial and circumferential inflow velocities at the location of SRV sections, $m \cdot s^{-1}$
V_∞	=	freestream velocity, $m \cdot s^{-1}$
V^*	=	resultant inflow velocity of SRV sections; $\sqrt{(V_a + v_a)^2 + (V_t + v_t)^2}$, $m \cdot s^{-1}$
v_a, v_t	=	axial and circumferential induced velocities by SRVs, $m \cdot s^{-1}$
X	=	samples in optimization process
x, y	=	axial and spanwise coordinate, m
Γ	=	circulation, $m^2 \cdot s^{-1}$
μ	=	doublet strength, $m^3 \cdot s^{-1}$
ρ	=	air density, $kg \cdot m^{-3}$
τ	=	twist angle, deg
φ	=	SRV azimuthal position, deg
σ	=	source strength, $m^2 \cdot s^{-1}$
Φ	=	velocity potential, $m^2 \cdot s^{-1}$
Ω	=	position vector, m

Subscripts

P	=	propeller
V	=	swirl recovery vane
W	=	wing

I. Introduction

GROWING demand for air-based transport [1] and the subsequent environmental impact [2] have raised great challenges to airlines [3], and therefore aircraft and engine manufactures, of providing aircraft with lower fuel consumption, lower noise production, and less emissions than what the current technology provides. Turboprop propulsion systems, with their advantage of higher propulsive efficiency compared with equivalent technology level turbofan engines [4], are considered a suitable technology to provide low emission propulsion of airplanes. In the short-haul sector below 400 nautical miles, turboprops are dominant choice as their market share is around 75% [5]. In the large regional aircraft segment (60–90 seats) of in-service fleet, turboprop engines and turbojet engines share the market evenly since the year of 2003 according to the statistics published by Bombardier Aerospace [6]. Moreover, the commercial turboprop aircraft manufacturers such as ATR and Bombardier initiated a new focus on the 90–120 seats segment market where the turbojet-powered aircraft is so far the only choice [7].

Because propeller propulsion has a long history in aviation, many studies have been performed on its integration with other aircraft components. It was recognized that the aerodynamic interaction between the propeller and other aerodynamic surfaces produces both time-averaged and unsteady loads that have an effect on the aircraft

---

Presented as Paper 2018-3648 at the 2018 Applied Aerodynamics Conference, Atlanta, GA, 25–29 June 2018; received 4 July 2018; revision received 29 October 2018; accepted for publication 29 October 2018; published online 2 January 2019.

*Ph.D. Candidate, Flight Performance and Propulsion Section, Faculty of Aerospace Engineering. Member AIAA.

†M.Sc., Flight Performance and Propulsion Section, Faculty of Aerospace Engineering.

‡Full Professor, Flight Performance and Propulsion Section, Faculty of Aerospace Engineering. Member AIAA.

§Full Professor, Head of Flight Performance and Propulsion Section, Faculty of Aerospace Engineering. Member AIAA.

aerodynamic performance, stability and control, structural loading, and production of noise and vibration [8]. Among many investigations of the tractor propeller effect on the wing performance, Kroo [9] and Miranda and Brennan [10] demonstrated numerically that reduction of lift-induced drag can be achieved by propeller-wing interaction due to the recovery of the angular momentum (swirl) in propeller slipstream by the trailing wing. This conclusion was verified experimentally for tractor-propeller configurations by Witkowski et al. [11]. Numerical effort was also undertaken in Witkowski's work to determine the wing load dependence on parametric variations, which led to basic understandings of wing swirl recovery in tractor configurations. As pointed out by Veldhuis [12], further improvement in induced-drag reduction performance can be obtained by properly adapting the wing loading distribution immersed in the slipstream.

In an attempt to improve the propulsive efficiency of propellers, swirl recovery vanes (SRVs) (as shown in Fig. 1) were introduced, which are capable of recovering swirl in the slipstream and thus generate extra thrust [13,14]. This was proposed by NASA in the late 1980s as part of the Advanced Turboprop Project. Experimental data showed an extra 2% of propeller thrust generated by SRVs at the design condition of $Ma = 0.8$ [15]. Recently, numerical design of SRVs was performed by Wang et al. [16] and Stokkermans et al. [17] of which the results have indicated order of 2–5% extra thrust from SRVs at relatively high propeller-loading conditions. In the authors' previous work [18], a hybrid SRV design framework based on a lifting-line model was developed. A set of SRVs with a blade count of four was designed. The design was subsequently validated in a wind-tunnel experiment. At the design condition of propeller advance ratio $J = 0.6$ and thrust coefficient $C_{T,P} = 0.32$, an extra 3.4% of propeller thrust was predicted by the numerical design, and 2.6% was measured in the wind-tunnel tests. The thrust coefficient of the SRVs showed an approximately linear relation with the propeller thrust coefficient, diminishing to 1.5% of the propeller thrust at $C_{T,P} = 0.20$ based on the experimental results. A study on SRV application in wing-mounted tractor-propeller configuration was carried out by Stokkermans [19]. In this study, SRVs designed for isolated propeller were investigated in wing-mounted configuration by means of Reynolds-averaged Navier–Stokes (RANS) simulations. Results showed that the SRVs performance degrades significantly due to flow separation caused by wing-induced velocities. However, by manually adjusting the pitch angle of the vanes in RANS simulations, benefit was gained in terms of either improved wing performance or system propulsive efficiency. This implies that an integrated SRV design taking the wing effect into account will most likely result in a performance benefit in practice.

As demonstrated by Witkowski et al. [11], the reduction of the wing drag due to propeller-wing interference originates from the tilting of the lift force by the swirl velocity in the propeller slipstream.

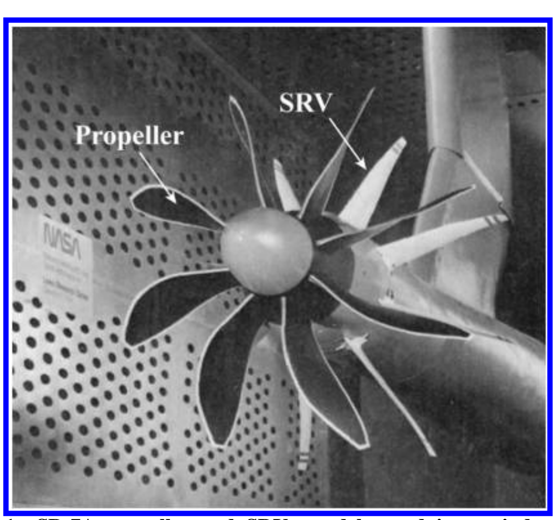

Fig. 1 SR-7A propeller and SRVs model tested in a wind tunnel (adapted from Dittmar and Hall [14]).

The lift force acting on the wing in the propeller-induced upwash region exhibits a augmentation (due to an increment of the local incidence angle) and forward rotation, leading to a negative drag force contribution. Similarly, in the downwash region, the lift force is diminished (due to decrease of incidence angle) and rotated backward, producing components of positive drag. When SRVs are introduced in the slipstream, both the magnitude and azimuthal distribution of swirl velocity will be changed in front of the wing so that the tilting of aerodynamic force on the wing will be changed correspondingly. Therefore, an integrated design should be performed combining both thrust production from the vanes and induced-drag reduction from the wing.

Although SRV design for maximum thrust and wing optimization for minimum induced-drag have been investigated separately, it has not been studied yet whether it is beneficial to combine these two components. No research has been performed on how to integrate SRVs with a wing that employs a propeller propulsion system. The current research is conducted to fill this gap. The methodology used for the design and analysis of SRVs and wing is first introduced in Sec. II. The case study of swirl recovery by wing-shape optimization is detailed in Sec. III. The swirl recovery performance by adding SRVs in the corresponding wing-installed tractor propeller configuration is provided in Sec. IV.

II. Methodology

Because there are three components in the tractor propeller-SRV-wing system, three modules in the design procedure are established correspondingly. These three modules are 1) the analysis module of the isolated propeller to establish the flowfield of slipstream, 2) the SRV design module in the propeller-wing-induced velocity field, and 3) the wing analysis module in the propeller-SRV-induced velocity field. The modular design process of swirl recovery system is shown in Fig. 2.

Before the design of swirl recovery system, a description of the velocity field induced by the propeller is required. This is achieved by performing a numerical simulation of the isolated propeller based on RANS equations. In installed configuration, as discussed by Veldhuis [12], the effect of the wing loading on the inflow field of a tractor propeller is similar to the impact of an incidence angle on an uninstalled propeller. Each of the blades generates an unsteady load that is dependent on the azimuthal position in the rotation cycle. However, the experimental results from Ortun et al. [20] showed that the time-averaged thrust and torque coefficients of the propeller in incidence exhibit negligible change when the inclination angle is smaller than 2 deg. Furthermore, because the objective of this paper is to compare the swirl recovery performance from the wing and the SRVs, it is necessary to have the same velocity input for both cases. Because of the two reasons discussed above, during the design process of swirl recovery system, the amount of the swirl in the slipstream is assumed to be constant by neglecting the perturbations of propeller performance due to the addition of the SRV and the wing.

With respect to SRV and wing design, a multifidelity optimization algorithm is used. A potential flow-based analysis is adopted as low-fidelity method for fast convergence. The solutions to the Euler equations are used as high-fidelity method for higher accuracy of performance determination of the whole system. The multifidelity optimization is a double-loop process including an inner loop and an outer loop. The inner loop corresponds to a lift-constrained drag-minimization problem performed with low-fidelity method, and the outer loop corresponds to an alignment procedure between the low-fidelity model and high-fidelity model using a correction algorithm. The details of each design/analysis module and the optimization process are described as follows.

A. Propeller Slipstream Setup

The propeller used in this research represents a scaled model of a conventional propeller of a typical regional turboprop aircraft. It features six blades and a radius of 0.2032 m. The hub of the propeller has a radius of 0.042 m, and the blade pitch angle equals 50 deg at 70% of the radius. The geometric details of the propeller are

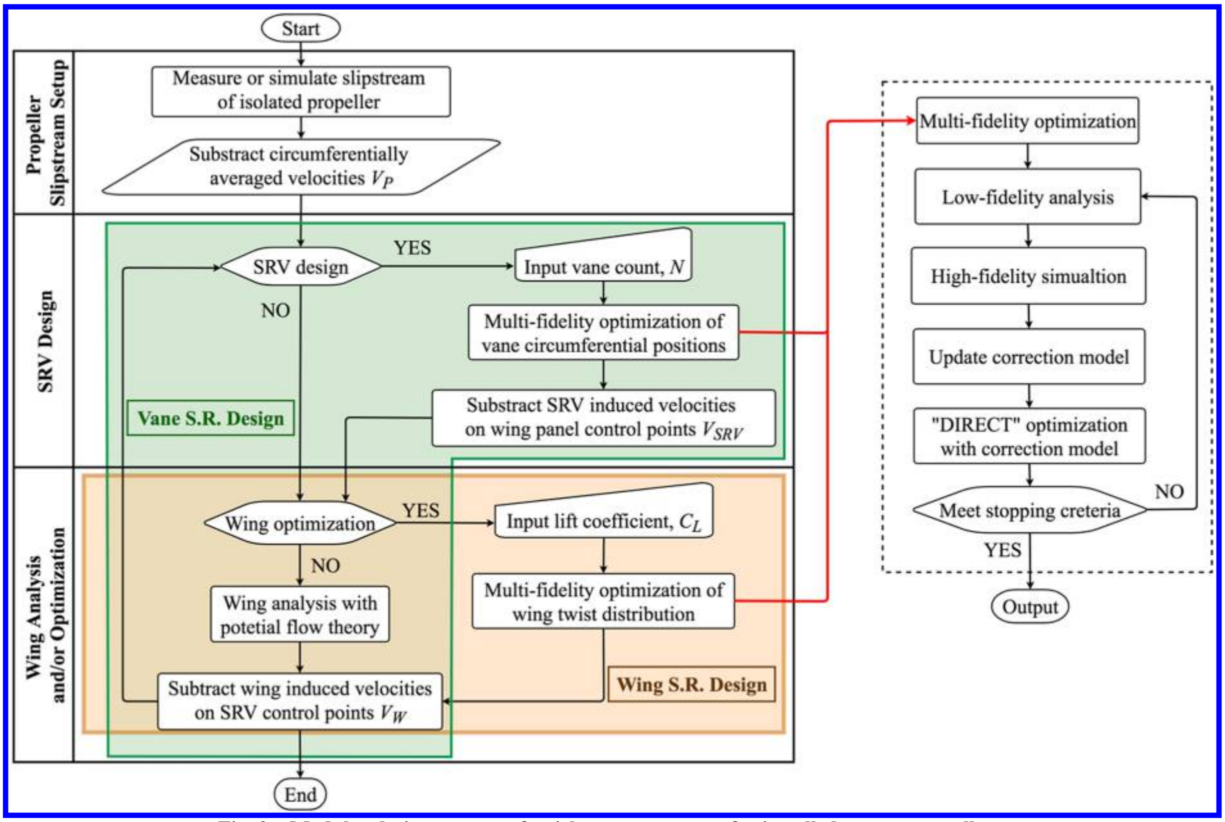

Fig. 2 Modular design process of swirl recovery system for installed tractor propellers.

described in Fig. 3. The propeller is positioned at zero incidence angle relative to the freestream velocity.

The computational mesh for the RANS simulation of the isolated propeller is the same as that was used in Ref. [18], where a grid refinement study was performed and the simulation results were validated by experimental data in terms of both the propeller performance coefficients and the velocity distributions in the propeller slipstream. Because the current case is performed at more benign conditions (lower thrust coefficient and higher Reynolds number) compared with the previous validation, no new validation was considered as necessary. The simulation in the current study is carried out at the cruise condition of a typical turboprop aircraft, which corresponds to an altitude of 5000 m and flight Mach number of 0.44 [21]. The propeller operates at an advance ratio J of 2.4 and a computed thrust coefficient $C_{T,P}$ of 0.22. It should be noted that the operating cases at lower flight speeds (e.g., take-off or climb) are not investigated in this study.

The radial distributions of the circumferentially averaged axial velocity V_a and tangential velocity V_t produced by the propeller are critical input information for SRV and wing design. In Fig. 4, the axial development of the velocity distributions is depicted on five survey planes perpendicular to the propeller axis. Their axial distance to the propeller plane ranges from $0.5R$ to $2.5R$. It can be observed that the distributions of V_t exhibit a negligible change when the slipstream

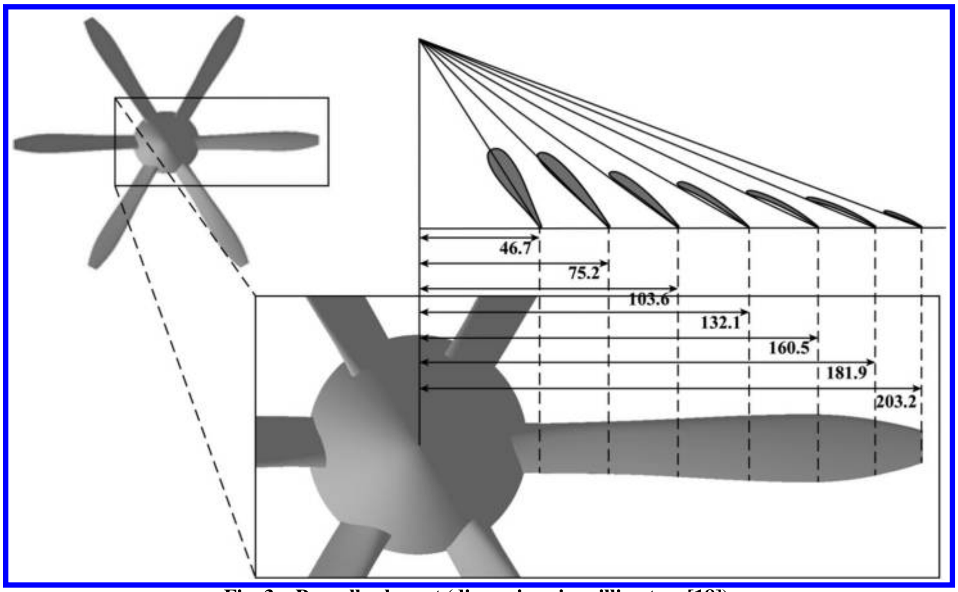

Fig. 3 Propeller layout (dimensions in millimeters [18]).

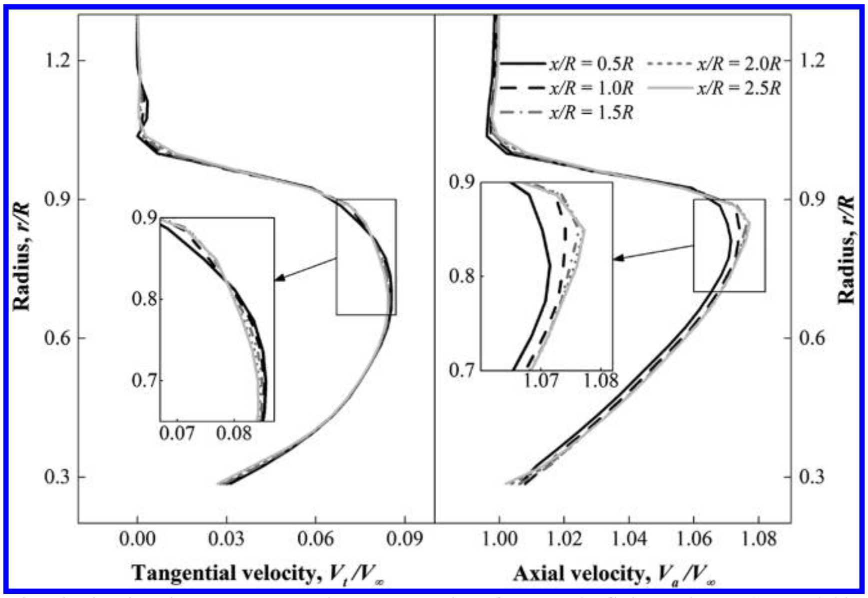

Fig. 4 Velocity distributions in the propeller slipstream obtained from a RANS simulation at $C_{T,P} = 0.22$ and $J = 2.4$.

develops downstream, whereas the axial velocity increases along the axis up until the plane at $x/R = 1.5R$ and keeps constant afterward.

B. Low-Fidelity Potential Flow-Based Analysis of Propeller-SRV-Wing Configuration

The flowfield of propeller slipstream is determined by a RANS simulation of the isolated propeller as discussed above, and the circumferentially averaged velocity distributions in the slipstream are taken as input information for SRV and wing design. A lifting line model is used for SRV design and a surface singularity method is used for wing performance analysis. A full coupling between SRV design and wing analysis is established where iterations are performed until both are converged. However, the deformation of the propeller slipstream due to its interaction with either SRV or wing has been neglected in the potential flow-based analysis.

1. SRV Design with Circumferentially Nonuniform Inflow

A design procedure of SRVs for isolated propeller was established in the authors' previous work [18] based on a lifting-line model. From time-averaged point of view, the velocity field behind the isolated propeller is circumferentially uniform. Hence, the SRVs designed for an isolated propeller are uniformly distributed along the azimuthal direction, and all of the vanes have the same loading distribution. However, in installed configuration, the circumferential uniformity is altered by the wing-induced velocities. The design procedure of SRVs is thus adapted in the way that, first, the vane loadings are uniquely dependent on their azimuthal positions with specific inflow velocities and, second, the azimuthal positions of the vanes (φ_i) are optimized for maximum thrust production.

For determination of φ_i, the global optimization algorithm DIRECT (abbreviation of "DIviding RECTangles") is used, which will be introduced later in Sec. II.D. With the azimuthal positions fixed, the determination of the optimum loading distributions of the vanes is required. The inflow velocities at vane positions are obtained by summation of freestream velocity and velocities induced by the propeller and the wing. Following the terms used previously in Ref. [18] and the force diagram shown in Fig. 5, the SRV thrust is determined by the Kutta-Joukowski's theorem and can be expressed as:

$$T_V = \rho N \sum_{n=1}^{N} \sum_{m=1}^{M} \left(\left(V_{t_{m,n}} + v_{t_{m,n}} \right) \Gamma_{m,n} - \frac{1}{2} V^*_{m,n} C_{d_{m,n}} c_{m,n} \left(V_{a_{m,n}} + v_{a_{m,n}} \right) \right) \Delta r_{m,n} \tag{1}$$

where N is the total blade count, n is the index of blade count, M is the total number of lifting segments in lifting line theory, and m is the index

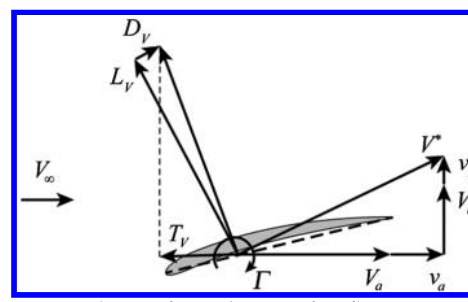

Fig. 5 Velocity and force diagram of an SRV blade section.

of each lifting segment. To have maximum thrust, the partial derivative of T_V with respect to the circulation distribution is set to zero:

$$\frac{\partial T_V}{\partial \Gamma_{m,n}} = 0 \tag{2}$$

where the derivative is given by:

$$\begin{aligned} \frac{\partial T_V}{\partial \Gamma_{m,n}} = {} & \left(V_{t_{m,n}} + v_{t_{m,n}} \right) \Delta r_{m,n} + \sum_j \sum_i \frac{\partial v_{t_{i,j}}}{\partial \Gamma_m} \Gamma_{i,j} \Delta r_{i,j} \\ & - \sum_j \sum_i \frac{1}{2} \frac{\partial V^*_{i,j}}{\partial \Gamma_m} C_{d_{i,j}} c_{i,j} \left(V_{a_{i,j}} + v_{a_{i,j}} \right) \Delta r_{i,j} \\ & - \sum_j \sum_i \frac{1}{2} V^*_{i,j} \frac{\partial \left(C_{d_{i,j}} \cdot c_{i,j} \right)}{\partial \Gamma_m} \left(V_{a_{i,j}} + v_{a_{i,j}} \right) \Delta r_{i,j} \\ & - \sum_j \sum_i \frac{1}{2} V^*_{i,j} C_{d_{i,j}} c_{i,j} \frac{\partial v_{a_{i,j}}}{\partial \Gamma_m} \Delta r_{i,j} \end{aligned} \tag{3}$$

As shown in Ref. [18], the distributions of the sectional drag coefficient C_d and chord length c have negligible effect on the optimum circulation distribution. Thus, the terms including either C_d or c on the right-hand side of Eq. (3) diminish and Eq. (2) can be rewritten as:

$$\frac{\partial T_V}{\partial \Gamma_{m,n}} = \left(V_{t_{m,n}} + v_{t_{m,n}} \right) \Delta r_{m,n} + \sum_j \sum_i \frac{\partial v_{t_{i,j}}}{\partial \Gamma_m} \Gamma_{i,j} \Delta r_{i,j} = 0 \tag{4}$$

The partial derivatives of the induced tangential velocities with respect to the circulations of the horseshoe vortices are computed by Biot–Savart's law. A nonlinear system of equations is formulated with the circulation strength of the vane lifting segments as independent variables. The system of equations is solved by Newton's method.

Once the bound circulation distributions of the vanes are determined, the induced velocities from the vanes on the wing collocation points can be calculated using Biot–Savart's law. In this process, the deformation of the slipstream due to the wing was not taken into account. To perform Euler simulation, the vane shapes also need to be determined. It should be noted that with a prescribed circulation distribution, there are infinite numbers of vane shape that can achieve this distribution. The one used in this paper employs a NACA 2412 airfoil shape. The chord length of the vane sections is proportional to their local circulations, and the maximum chord length equals that of the propeller root. The local incidence angle of the vane sections is adjusted to maintain the desired circulation distribution.

2. Wing Analysis with Surface Singularity Method

The wing performance is obtained with potential flow-based surface singularity method considering interaction effects from the propeller and SRVs.

a. Potential Flow Formulation. When the flow surrounding the wing is assumed to be inviscid, irrotational, and incompressible, a scalar velocity potential Φ_{Total} can be defined such that the continuity of mass is governed by the Laplace's equation as:

$$\nabla^2 \Phi_{\mathrm{Total}} = 0 \tag{5}$$

Following Green's identity, applying the boundary element discretization of Laplace's equation to a traditional wing geometry results in the following integrals for calculating the perturbation potential from the wing ($\Phi_W = \Phi_{\mathrm{Total}} - \Phi_\infty - \Phi_P - \Phi_V$):

$$\Phi_W = \frac{1}{4\pi} \int_{S_{\mathrm{bound}}+S_{\mathrm{wake}}} \mu \frac{\partial}{\partial \boldsymbol{n}} \left(\frac{1}{\|\Omega\|} \right) \mathrm{d}S - \frac{1}{4\pi} \int_{S_{\mathrm{bound}}} \sigma \left(\frac{1}{\|\Omega\|} \right) \mathrm{d}S \tag{6}$$

By applying Dirichlet boundary condition, the internal potential is set to zero as:

$$\frac{1}{4\pi} \int_{S_{\mathrm{bound}}} \mu_b \frac{\partial}{\partial \boldsymbol{n}} \left(\frac{1}{\|\Omega\|} \right) \mathrm{d}S - \frac{1}{4\pi} \int_{S_{\mathrm{bound}}} \sigma \left(\frac{1}{\|\Omega\|} \right) \mathrm{d}S + \frac{1}{4\pi} \int_{S_{\mathrm{wake}}} \mu_w \frac{\partial}{\partial \boldsymbol{n}} \left(\frac{1}{\|\Omega\|} \right) \mathrm{d}S = 0 \tag{7}$$

where the wake potential jump μ_w is determined by a Kutta condition imposed at the trailing edge of the lifting surface. The wake is prescribed as a drag-free wake of which the panels are aligned with the freestream velocity. Setting up source strength to:

$$\sigma_i = \boldsymbol{n}_i \cdot (\boldsymbol{V}_\infty + \boldsymbol{V}_{P,i} + \boldsymbol{V}_{V,i}) \tag{8}$$

results in the value of the doublets as unknowns.

b. Panel Pressure and Force. Once the strength of surface singularities is determined, the velocity induced by the wing is computed by calculating the gradient of the doublet distribution. The pressure on the wing surface can be obtained through Bernoulli's equation. To account for the compressibility effect, the Prandtl–Glauert correction is applied, and the pressure coefficient is given as:

$$C_{p,i} = \left(1 - \frac{(\boldsymbol{V}_\infty + \boldsymbol{V}_{P,i} + \boldsymbol{V}_{V,i} + \boldsymbol{V}_{W,i})^2}{(\boldsymbol{V}_\infty + \boldsymbol{V}_{P,i} + \boldsymbol{V}_{V,i})^2} \right) \Big/ \sqrt{1 - Ma_\infty^2} \tag{9}$$

The aerodynamic force on the panel can be computed as:

$$\Delta \boldsymbol{F}_i = -C_{p,i} \left[\frac{1}{2} \rho (\boldsymbol{V}_\infty + \boldsymbol{V}_{P,i} + \boldsymbol{V}_{V,i})^2 \right] \Delta S_i \boldsymbol{n}_i \tag{10}$$

The total force of wing is then obtained by integrating the forces of all the wing surface panels.

c. Induced Drag Calculation by Trefftz-Plane Analysis. The induced drag of the wing is calculated by a far-field method in the so-called Trefftz-plane. This method has been proven by many authors to be capable of providing accurate predictions of the induced drag [22,23]. The calculation can be accomplished by virtue of Kutta-Joukowski's theorem in the drag direction on the Trefftz-plane by calculating the line integral:

$$D_i = \frac{1}{2} \int \rho (\boldsymbol{V}_{P,i} + \boldsymbol{V}_{V,i} + \boldsymbol{V}_{W,i}) \cdot \boldsymbol{n}_i \Gamma_i \, \mathrm{d}l_i \tag{11}$$

Originating from three different sources of induced velocities on the wing, three components are identified: the wing self-induced drag (by $\boldsymbol{V}_W$), the propeller-induced drag (by $\boldsymbol{V}_P$), and the SRV-induced drag (by $\boldsymbol{V}_V$). The induced drag is computed by the method proposed by Blackwell [24]. It should be noted that the viscous drag of the wing is assumed to be constant, and thus it is not included in the optimization procedure.

C. High-Fidelity Euler Equation-Based Simulation of Propeller-SRV-Wing Configuration

As mentioned in Sec. II.B, in potential flow-based method, the deformation of the slipstream is neglected. This is done in order to achieve fast computation when performing optimization. However, as observed by Veldhuis [12], a strong deformation of the slipstream symmetry exists when the wing is given a positive angle of attack. The inaccuracy resulting from the neglecting of the slipstream deformation can be corrected by a higher-fidelity method that employs full coupling of the propeller slipstream, SRV, and wing. Because the aerodynamic theory used in potential flow method is inviscid, a natural choice for the higher-fidelity model is an Euler equation-based solver.

The propeller in Euler equation-based simulation is represented by an actuator disk in order to maintain the same velocity distributions in the slipstream as in those obtained from the RANS simulation. The radial distributions of the propeller thrust and torque obtained from the RANS simulation are replaced by axial and angular momentum sources in the actuator disk model. The resolution of the wing solid surface, the refinement of propeller slipstream region, wing wake, and wing tip vortex region are similar to that discussed by Lotstedt [25]. The same strategy is also applied to the vanes by scaling down the grid size based on the ratio of chord length of SRV and wing. The simulations are performed with the finite volume-based solver ANSYS® CFX.

D. Global Optimization by DIRECT Algorithm

The design of the swirl recovery system for propeller propulsion system is achieved by optimizing the summation of the thrust production from the vanes and the induced drag reduction of the wing, while maintaining total lift constant. The optimization problem can be stated as follows:

$$\begin{aligned} &\underset{X \in \Re^D}{\text{minimize}} && -C_{T,V}(X) + C_{D,i}(X) \\ &\text{subject to} && C_{L,W}(X) + C_{L,V}(X) = \text{const} \end{aligned} \tag{12}$$

The gradient-free DIRECT optimization algorithm is used to achieve global optimization, where DIRECT stands for "DIviding RECTangles" [26]. This algorithm, which was proposed by Jones et al. [26], is a modification of the standard Lipschitzian approach [27]. By identifying the potentially optimal intervals, the algorithm balances its effort between global and local searches of the objective function to guarantee a global optimum. The successful application of DIRECT algorithm in aerodynamic optimization has been reported by many authors [28–30]. This algorithm is found suitable for global optimization problems with bound constraints and a real-valued objective function when the objective function is a "black box" function or evaluation. The nonlinear constraint of the constant lift in Eq. (12) is treated implicitly during the optimization loop in the way that, for a given wing shape, the incidence angle of the wing is adjusted to acquire the desired total lift. Thus, the original nonlinear constraint optimization problem is relieved to a bound constraint optimization problem that can be solved by DIRECT optimization as:

$$\begin{aligned} &\underset{X\in\Re^D}{\text{minimize}} \quad -C_{T,V}(X) + C_{D,i}(X) \\ &\text{subject to} \qquad X \in [X_{\min}, X_{\max}] \end{aligned} \tag{13}$$

E. Multifidelity Optimization Using Shape-Preserved Response Prediction Algorithm

To reduce the number of evaluations of the high-fidelity models, a surrogate-based optimization (SBO) technique is used. The low-fidelity potential flow-based surrogates are corrected to become a reliable representation of the high-fidelity Euler equation-based model. By using the SBO technique, the optimization burden is shifted to the low-cost surrogate model, whereas the high-fidelity model is referenced occasionally for verification purposes only.

The model alignment of SBO is performed not directly to the figures of interests (response surfaces of $C_{T,V}$, $C_{D,i}$, $C_{L,W}$, and $C_{L,V}$), but to the intermediate simulation results, more specifically, the circulation distribution of the vanes, and the lift and circulation distributions of the wing. As the objective and constraint of the optimization problem are uniquely determined by these distributions, alignment of the corresponding distributions for the low- and high-fidelity models will result in an alignment of the objective and constraint. The shape-preserving response prediction (SPRP) methodology is adopted here for the model alignment.

In Fig. 6, an example of the application of SPRP alignment procedure on the wing circulation distribution is depicted. We denote the circulation distributions from the Euler solution and potential flow-based results as Γ_E and Γ_p, respectively. At the beginning of multifidelity optimization, the global optimization is carried out based on the low-fidelity method (so that Γ_p is obtained). The optimum design obtained from the low-fidelity optimization is then simulated by high-fidelity Euler solver (so that Γ_E is obtained). The SPRP alignment is established by determining the translation vectors of corresponding circulation distributions, that is, the difference between Γ_E and Γ_p. The model alignment between low fidelity and high fidelity is constructed, assuming that the change of Γ_E due to adjustment of the wing shape in the next iteration of global optimization can be predicted using the change of Γ_p. Thus, the SPRP model is applied to the low-fidelity analysis during the new iteration of global optimization. The formulations for the vane circulation and wing lift distribution are analogous.

III. Swirl Recovery Design of Trailing Wing for a Tractor Propeller

The swirl recovery by a trailing wing with a tractor propeller results in a reduction in wing-induced drag, of which the mechanism was

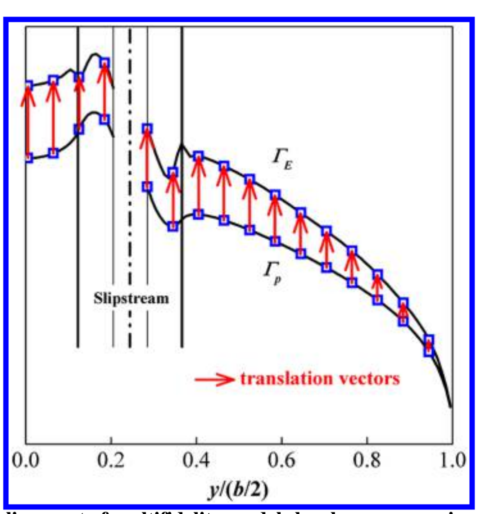

Fig. 6 Alignment of multifidelity models by shape-preserving response prediction methodology.

well explained by Witkowski et al. [11]. To achieve the lift distribution with minimum induced drag, the twist distribution of the wing is optimized. The distribution is represented by a B-spline curve with eight control points located at eight spanwise locations as shown in Fig. 7. The upper and lower bounds of twist angle are set to 0 and 8 deg, respectively (so that the range is larger than the maximum difference of the optimum twist angles). The wing is represented by singularities distributed on 200 spanwise panels and 23 chordwise panels. Because the lift and circulation distributions will be corrected by high-fidelity Euler solutions, these panel numbers are adequate to resolve the integrated loads ($C_{L,W}$ and $C_{D,i}$) within 0.1% of accuracy.

The wing geometry, which is shown in Fig. 8, is a scaled model of a typical turboprop aircraft, in this case the Fokker F50 [12]. The wing airfoil is NACA 64_2415 and assumed to be the same for all spanwise sections. The dihedral and twist of the original wing geometry are neglected for simplification. The fuselage is not considered as well and the half wing is extended to the full span. At cruise condition, the total lift coefficient equals 0.5, which is set as an implicit constraint during the twist optimization.

A. Convergence of Multifidelity Optimization

As illustrated in Fig. 2, the multifidelity optimization is a double-loop procedure. The inner loop is performed with DIRECT global optimization algorithm and stopped when the number of evaluations exceeds 100 times the number of design variables (which is 8 in this case). The outer loop is terminated when the difference of minimum induced drag between the current loop and the previous loop is less than 0.2 count.

The multifidelity optimization of wing twist distribution has converged after three outer loops. The convergence is shown in Fig. 9, where on the left the convergence history of each inner loop (DIRECT global optimization) is illustrated and on the right the optimum twist distributions of different inner loops are compared. The induced drag has decreased by 3.9 counts after optimization compared with that of the straight wing. This amount of drag reduction is equivalent to 1.4% of propeller thrust. The optimum twist distributions of three inner loops exhibit the same shape, which further confirms the convergence of the multifidelity optimization. In general, the optimum twist distribution is characterized by higher value inside the slipstream, and lower value at the tip. Because of the lift constraint, the loading is allocated more to the region where the lift-drag ratio is higher, which is the region immersed in the slipstream. The twist angle is lowest at the wing tip to reduce the strength of tip vortex and thus to reduce tip loss.

B. Design Space Exploration of Twist Distribution by DIRECT Algorithm

By balancing between global and local searches, the DIRECT algorithm is guaranteed to converge to the global optimum provided that the objective function is continuous [26]. Figure 7 illustrates the response surface of the wing-induced drag against twist angles at control points obtained from the third inner loop. It should be noted that each scatter point in this figure represents multiple samples in the optimization because, for a given combination of twist angles (τ_i, τ_j), there are multiple combinations of other twist angles (τ_k, $k = 1$–8 and $k \neq i$, j) evaluated during the optimization. Of all the samples, only the one with minimum response value is collected and shown in the contour.

It can be seen from Fig. 7 that the design space is fully explored and the response surfaces exhibit a single minimum. However, this does not mean that the twist optimization can be achieved by a gradient-based optimization algorithm with one starting point, because Fig. 7 only shows the response surface surrounding the global optimum and the actual response surface is multidimensional and unknown. The response variation with respect to the twist angles at the tip region (τ_7, τ_8) is much less compared with other control point locations. This indicates that the drag induced by the tip vortex is smaller than that induced by the slipstream, which will be confirmed and explained in the next section.

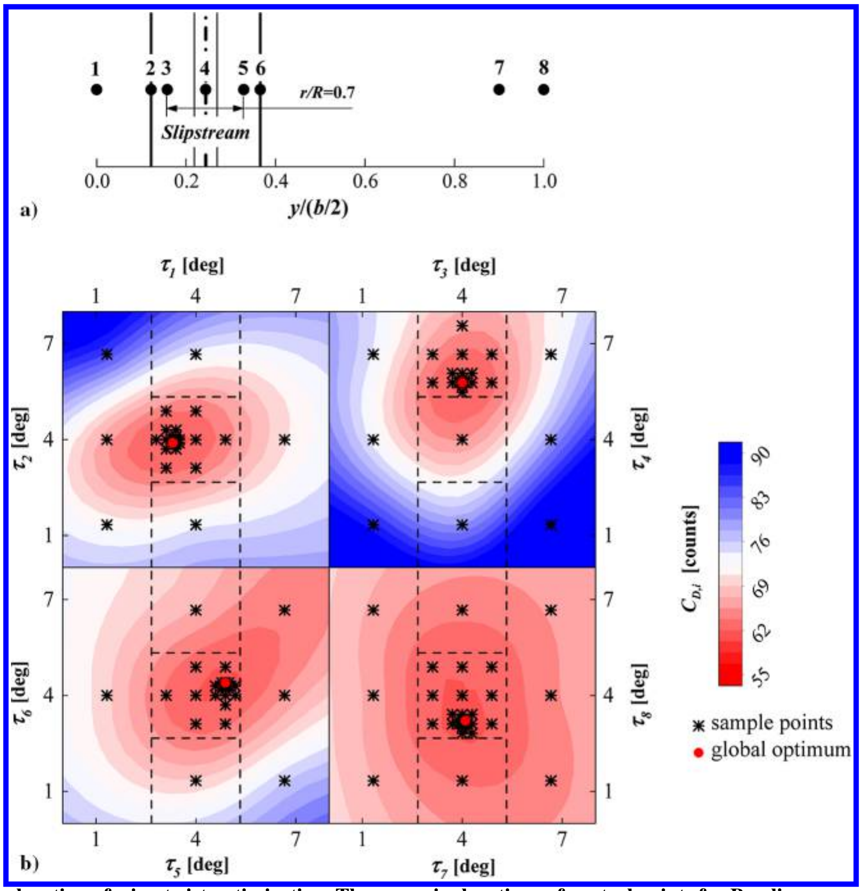

Fig. 7 Design space exploration of wing twist optimization. The spanwise locations of control points for B-spline curve are depicted at the top.

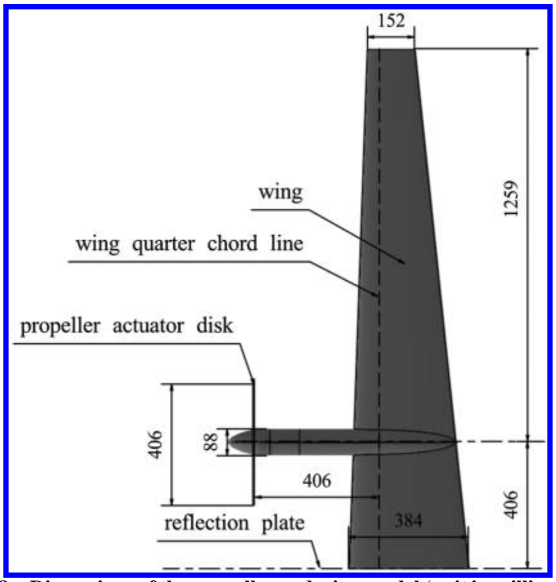

Fig. 8 Dimensions of the propeller and wing model (unit in millimeters, top view). The dimensions of the model are based on a scaled-down and simplified version of the Fokker 50 wing.

C. Optimum Spanwise Loading Distributions

Figure 10 presents the spanwise lift, circulation, and induced drag distributions of the wing with optimum twist distribution. In Figs. 10a and 10b, comparisons are made of the lift and circulation distributions obtained from potential flow-based analysis (denoted as potential), potential flow-based analysis applied with SPRP model (denoted as potential-SPRP), and the Euler simulation result (denoted as Euler). The match of both lift and circulation distributions between the latter two cases again confirms the convergence of the multifidelity optimization procedure.

The total induced drag, which includes the wing self-induced drag and the propeller-induced drag, is shown in Fig. 10c. The wing self-induced drag is a consequence of the downwash velocity produced by the trailing wake vorticity on the collocation points. Because the magnitude of local induced drag is proportional to the local strength of bound vorticity, the distribution of wing self-induced drag follows the same pattern of the circulation distribution in the way that the local maximum/minimum in circulation distribution results in local maximum/minimum of wing self-induced drag. Analogous to the downwash velocity induced by the trailing wake vorticity, the swirl velocity inside the propeller slipstream also induces (positive or negative) drag on the wing by tilting the lift force at wing collocation points. On the blade-upgoing side, the swirl velocity points upward and induces negative drag (or equivalently thrust) on the wing. Similarly, on the blade-downgoing side, the swirl velocity points downward and induces positive drag on the wing. Because the wing circulation is augmented on the blade-upgoing side and diminished on the blade-downgoing side, the propeller-induced negative drag is larger in magnitude than the positive drag. However, the propeller-induced drag cancels out each other on upgoing and downgoing sides, and the total reduction in drag, in the end, is small compared with the wing self-induced drag, accounting for only 4% of the total induced drag.

It can be seen from Fig. 10b that in the Euler simulation result, there is a local minimum in wing circulation distribution at the location of the slipstream edge on the blade-upgoing side, and a local maximum on the blade-downgoing side. These two extremes are not captured by the low-fidelity potential flow-based analysis. However, as discussed above, these extremes have a strong effect on the induced drag distribution. In this sense, it can be concluded that when performing the induced drag prediction of the wing with a tractor propeller, one should refer to a solution where the interaction between the propeller slipstream and the downstream wing is simulated.

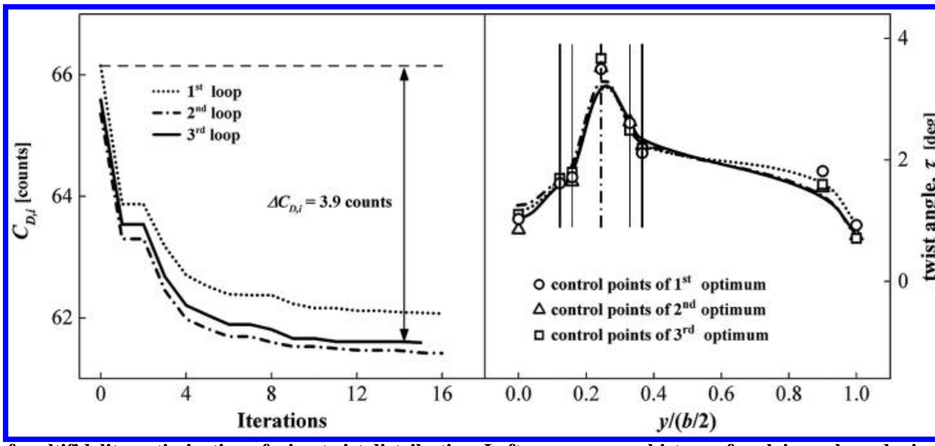

Fig. 9 Convergence of multifidelity optimization of wing twist distribution. Left: convergence history of each inner loop during DIRECT optimization. Right: comparison of optimum twist distributions to show convergence of the outer loop.

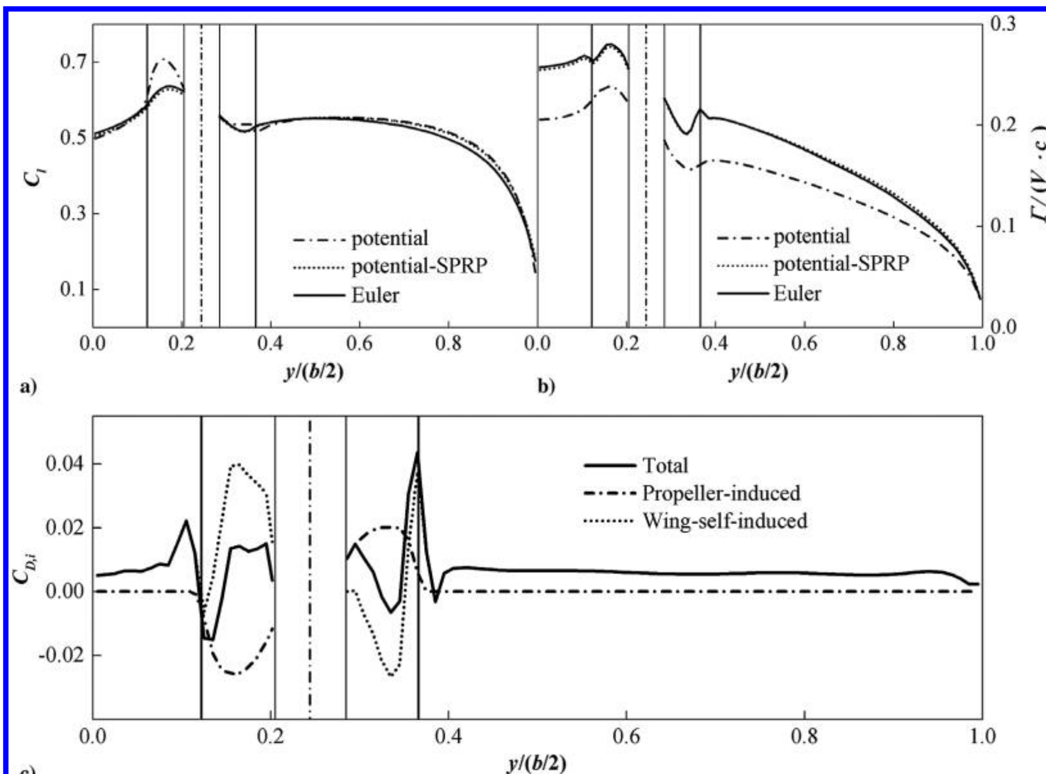

Fig. 10 Depiction of a) lift distribution, b) circulation distribution, and c) induced drag distribution of the wing with optimum twist distribution.

IV. SRV Design for Tractor Propeller in Installed Configuration

By optimizing the twist distribution of the wing, the reduction of induced drag can be achieved. However, the complexity of wing geometry and subsequently the difficulty in manufacturing has increased by introducing twist distribution. This problem can be tackled by having the wing without any twist distribution but introducing a set of SRVs that also have the capability of recovering swirl. In this way, extra thrust can be generated from the vanes. However, the velocity distributions inside the slipstream will be changed by the presence of SRVs. The lift and induced drag distributions of the wing will be altered accordingly. A full coupling between SRV design and wing analysis is established. A set of SRVs is designed at the same condition with that of the wing shape optimization.

The azimuthal positions of the vanes are optimized using DIRECT algorithm. The radius of the SRVs is kept the same as that of the propeller. The wing is again represented by singularities distributed on 200 spanwise panels and 23 chordwise panels, and SRVs are discretized into 20 lifting segments. The coupling between SRV design and wing analysis is defined to be converged when the change in SRV thrust is less than 1%, which corresponds to 0.02–0.05% of propeller thrust. This is considered as a sufficient resolution.

A. Effect of Axial and Azimuthal Positions of SRVs

1. *Velocity and Force Diagrams of SRVs and Wing*

The wing with a positive lift induces upwash at the front and downwash at the back, depending on the axial position relative to the wing. The angular velocity generated by the propeller, when expressed in wing coordinate system, points upward on the blade-upgoing side and downward on the blade-downgoing side, depending on the azimuthal position relative to the wing. Considering the installation position of SRVs, it can be either upstream or downstream of the wing in terms of axial position, and either on blade-upgoing side or

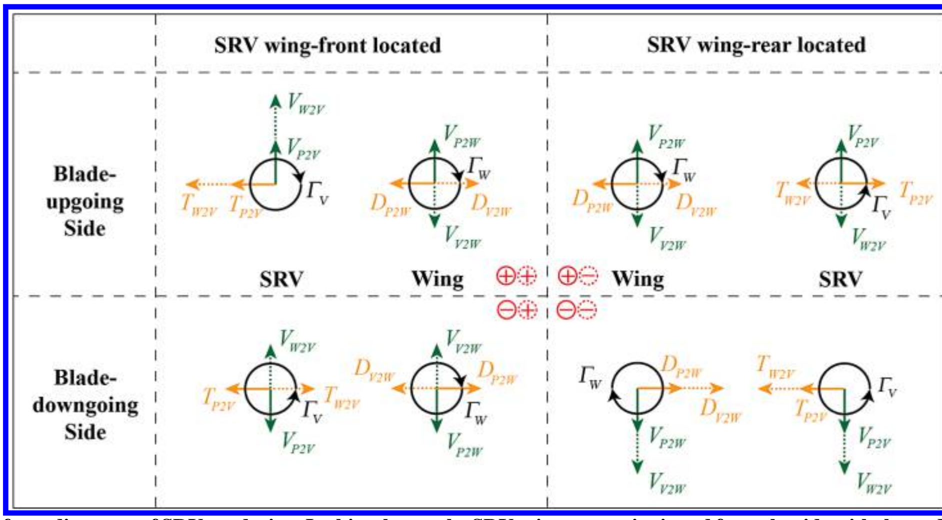

Fig. 11 Velocity and force diagrams of SRVs and wing. In this scheme, the SRV-wing system is viewed from the side with the undisturbed flow coming in from the left.

downgoing side in terms of azimuthal position. Consequently, the induced velocities from the propeller and wing on the SRVs are represented by four different cases, depending on the axial and azimuthal positions relative to the wing. Figure 11 illustrates the velocity and force diagrams of SRVs and wing of the four different cases.

On the blade-upgoing side, the upward angular velocity induced by the propeller is augmented by the wing-induced upwash when SRVs are located upstream of the wing, and reduced by the downwash when SRVs are located downstream of the wing. From SRV thrust production point of view, it is beneficial to locate SRVs upstream of wing. Besides positive thrust, SRVs also generate positive lift on this side. However, as will be discussed in the next section, the additional wing-induced drag produced by locating the SRVs upstream of the wing results in nonoptimal solution. On the blade-downgoing side, the downward angular velocity is decreased by the upwash upstream of wing, and enhanced by the downwash downstream of the wing. More thrust will be generated if SRVs are located downstream of the wing compared with the case where SRVs are located upstream of the wing. However, the lift force generated by the vanes is negative.

From the wing point of view, in all the four cases, the induced force on the wing by the SRVs always has the opposite direction with the induced force on the SRVs by the wing. This has a simple physical explanation when one notes that the swirl velocity in the propeller slipstream can either be recovered by the SRVs or the wing.

2. *Performance of SRV and Wing*

SRV design is performed at a blade count of $N = 1$ with different axial and azimuthal positions relative to the wing. The axial distance between SRV and the wing quarter-chord line is one time propeller diameter when SRV is located upstream of the wing, and three quarters of the wing root chord length ($x = 0.75c_r$) when SRV is located downstream of the wing. The thrust coefficient of SRV, $C_{T,V}$, the induced drag coefficient of the wing, $C_{D,i}$, and their summation are shown in Fig. 12. The azimuthal angle of SRV, φ, is defined as 0 and 180 deg when the vane is in vertical position and points upward/downward, respectively, whereas 90 and 270 deg indicate the vane in their horizontal position on the blade-downgoing and blade-upgoing side, respectively. The propeller actuator disk, the wing, and the optimum SRV design of four cases are sketched in Fig. 13.

When the SRV is located upstream of the wing, as discussed previously, it generates more thrust on the blade-upgoing side than on the blade-downgoing side. The maximum thrust provided by the vane equals 10.8 counts at the position of $\varphi = 309$ deg. However, the induced drag of the wing has increased dramatically mainly due to two reasons. First, as can be seen from Fig. 11 for the case where the SRV is located upstream of the wing on the blade-upgoing side, it induces downwash and thus positive drag on the wing. The wake

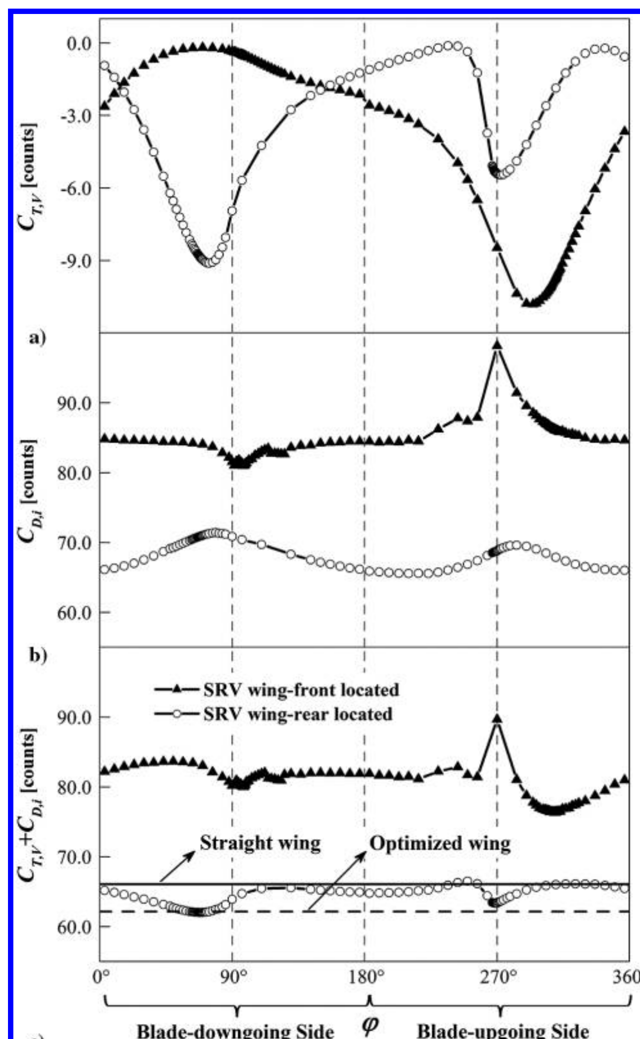

Fig. 12 SRV and wing performance with respect to different axial and azimuthal positions of SRV relative to the wing at $N = 1$; a) thrust coefficient of SRV $C_{T,V}$; b) drag coefficient of wing $C_{D,i}$; c) summation of $C_{T,V}$ and $C_{D,i}$.

vortices shed from the SRV is at a closer distance to the wing surface compared with the bound vorticity of SRV, and hence they become dominant in generating downwash velocities on the wing collocation points. Second, even though the rolling up of the vane tip vortex is not

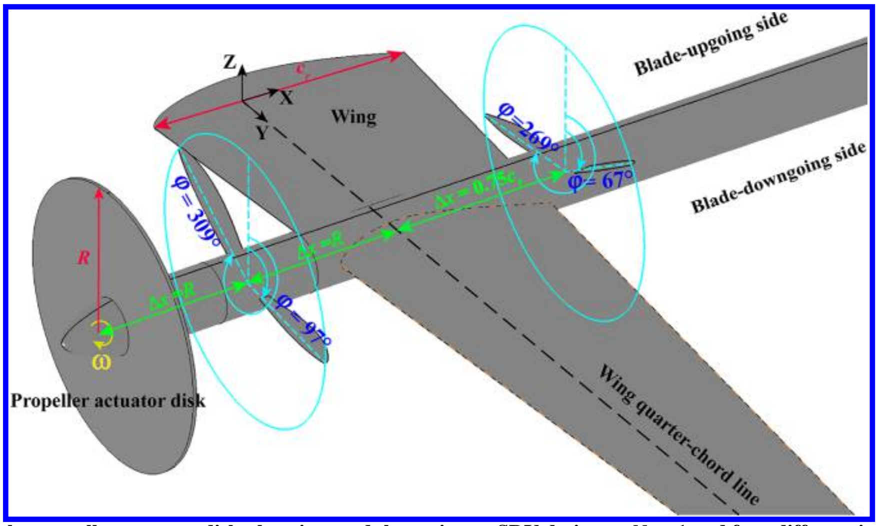

Fig. 13 Sketch of the propeller actuator disk, the wing, and the optimum SRV design at $N = 1$ and four different installation positions.

simulated in the lifting line model, it is captured by Euler simulation due to its inherent potential-flow cause of formation. Because of the rolling up of the vane tip vortex, the wing circulation exhibits an increase at the region close to the vane tip vortex. A local maximum is present in wing circulation distribution and consequently a local maximum in wing-induced drag. By multifidelity optimization algorithm, this effect is included in the induced drag evaluation of the wing. These two effects get their maximum influence at a vane position of $\varphi = 270$ deg as can be observed in Fig. 12b. For the reason discussed above, the increased amount of wing-induced drag is even higher than the thrust produced by the SRV. It is thus detrimental in terms of drag reduction to locate the SRV upstream of the wing.

When the SRV is located downstream of the wing, the angular velocity in propeller slipstream is enhanced by the wing-induced downwash on the blade-downgoing side. SRV gets its maximum thrust coefficient of 9.1 counts at $\varphi = 74$ deg. On the blade-upgoing side, a local maximum of $C_{T,V}$ is found when the SRV is located horizontally at $\varphi = 270$ deg where the wing-induced velocity gets its maximum. Because the wing is located upstream of SRV, both the wake and the tip vortices of the vane have limited effect on the wing loading distribution. There is maximum change of 5.8 counts of wing-induced drag with different vane azimuthal positions. The main reason for the change of wing-induced drag is that, besides thrust, the vane is also generating negative lift. To keep the total lift constant, the wing needs to provide more lift compared with the case without SRV. The summation of SRV thrust $C_{T,V}$ and wing-induced drag $C_{D,i}$ gets its minimum value of 62.0 counts at vane position of $\varphi = 67$ deg. At this position, the vane is capable of providing thrust of 8.8 counts. Hence, one may conclude that it is preferable to locate SRV downstream of wing on the blade-downgoing side to maximize of thrust production.

3. *Effect of Vane Axial Position Downstream of the Wing*

An optimum SRV location is identified in the discussion of previous section where the vane is located on the blade-downgoing side downstream of the wing. The effect of the vane axial position relative to the wing is investigated in this configuration at $N = 1$. The axial distance between the SRV and the wing is increased based on the case discussed in the previous section ($x = 0.75c_r$). The performance of SRV and wing is shown in Fig. 14. When increasing their axial distance, the induced velocity from the wing on the vane decreases. With less enhancement of angular velocity by the wing, less thrust is generated by the vane. Even though the induced drag of the wing also decreases, the drag of the combination increases. Thus, the system performance gets its optimum when SRV is located closest to the wing.

B. Effect of Blade Count

In the authors' previous work [18], it was found that the optimal number of SRVs with maximum thrust for isolated propeller case is $N = 9$. In the previous section, it is demonstrated that it is preferable

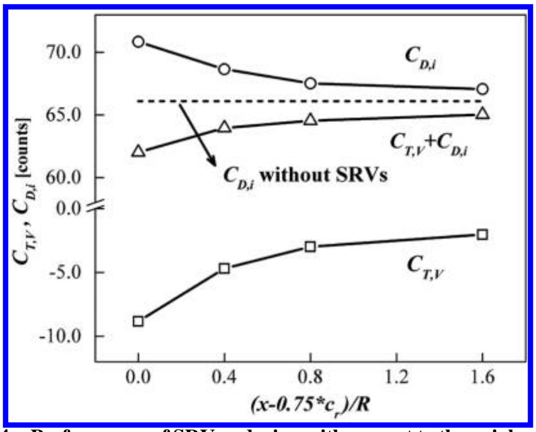

Fig. 14 Performance of SRV and wing with respect to the axial position of the vane downstream of the wing.

to locate SRVs on the blade-downgoing side downstream of the wing in the installed case. Even though there is a local optimum of system performance on the blade-upgoing side, the vane is located horizontally parallel to the wing such that the wake shed from the wing will impinge on the vane. This makes the local optimum questionable when taking viscous effects into account. Thus, the effect of blade count is investigated only on the blade-downgoing side with blade count up to 4. The system performance is depicted in Fig. 15.

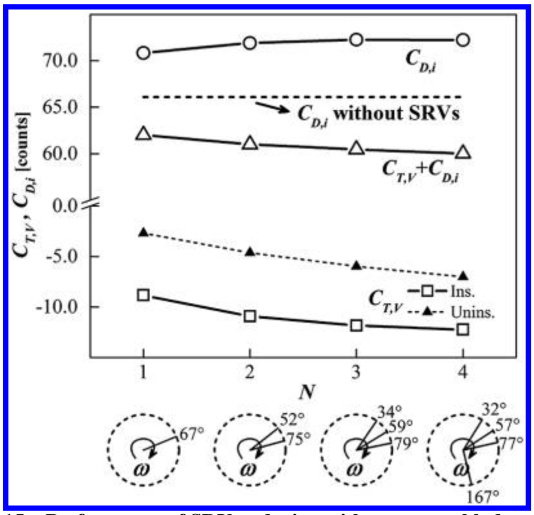

Fig. 15 Performance of SRV and wing with respect to blade count.

The induced drag of the wing again is correlated to the thrust of the SRVs because the wing needs to compensate for the negative lift produced by the vanes. Thus, the induced drag of the wing has increased by 1.4 counts when the vane count increases from 1 to 4.

The thrust coefficient of SRVs designed for both isolated propeller (uninstalled case, denoted as Unins.) and installed propeller (denoted as Ins.) is characterized in Fig. 15. In both cases, SRV thrust increases with the blade count. However, the thrust in the installed case is much larger than that of the uninstalled case (8.8 counts compared with 2.7 counts at $N = 1$). This is due to the swirl velocity enhancement by the wing on the blade-downgoing side. At $N = 4$ of the installed case, SRVs are capable of producing thrust of 12.2 counts, which is equivalent to 4.3% of propeller thrust. However, it should be noted that the viscous drag of the vanes is not taken into account in the inviscid analysis. The summation of $C_{T,V}$ and $C_{D,i}$ equals 60.0 counts at $N = 4$. Compared with the case without SRVs ($C_{D,i} = 66.1$ counts), the drag of the system has decreased by 6.1 counts.

V. Conclusions

Design of swirl recovery vanes (SRVs) for a propeller propulsion in tractor configuration at cruise conditions is performed numerically. The swirl recovery can be used either by the trailing wing or by introducing a set of SRVs in the slipstream. A design framework has been developed that consists of three modules corresponding to three components in this system: the analysis module of the isolated propeller, the SRV design module, and the wing analysis module. The design framework is based on a multifidelity optimization procedure. A potential flow-based method is adopted as the low-fidelity method for fast convergence, whereas an analysis based on Euler equations is used as the high-fidelity method. The DIRECT optimization algorithm is used for global optimization, and the shape-preserving response prediction methodology is adopted as the model alignment technique between low- and high-fidelity models.

A case study is carried out at the cruise condition of a typical turboprop aircraft. Two configurations are considered. In the first configuration, swirl recovery is achieved by the trailing wing, and the twist distribution of the wing is optimized. The Euler simulation of a tractor propeller-wing combination indicates that the slipstream impinging on the wing surface introduces local maxima and minima in wing circulation not only inside but also at the edge of the slipstream. The low-fidelity potential flow-based method is not able to capture the multiple extrema in the wing circulation distribution, making the multifidelity optimization technique necessary for all the analyses performed in this paper.

In the optimized wing configuration, the induced drag reduction is achieved by increasing the wing loading of the spanwise part where the lift to drag ratio is high, which is the region immersed in the slipstream. The twist angle is lowest at the tip to reduce the strength of wing tip vortex and thus tip losses. Compared with the original wing, the induced drag of the wing with optimum twist distribution has decreased by 3.9 counts out of 66.1 counts, corresponding to 1.4% of propeller thrust.

In the second configuration, a set of SRVs is introduced in the propeller slipstream. SRVs are designed with the constraint of constant total lift from SRVs and wing. Four different cases of SRVs installation positions are identified based on different axial positions (upstream and downstream the wing) and azimuthal positions (blade-upgoing side and blade-downgoing side) of SRVs relative to the wing. On the blade-downgoing side upstream of the wing and the blade-upgoing side downstream of the wing, the angular velocity in the slipstream is decreased by the wing induced velocity, whereas on the blade-upgoing side upstream of the wing and the blade-downgoing side downstream of the wing, the angular velocity is enhanced by the wing. From a thrust production point of view, it is beneficial to locate SRVs in regions where the angular velocity is enhanced. However, when SRVs are located upstream of the wing, the wake and tip vortices of the vane deteriorate the wing performance by increasing its induced drag. In such case, the thrust produced by the SRVs is counteracted by a larger drag increment on the wing. However, when the SRVs are located downstream of the wing, the circulation distribution of the wing is not disturbed much by SRVs, so as the induced drag. The best performance is found when the SRV is positioned on the blade-downgoing side downstream of the wing.

For the optimum configuration, a parameter study is performed in terms of the axial distance between SRV and wing. The system performance is found to be optimal when the SRV is located closest to the wing. At this position (where the SRV is three quarters of wing root chord length behind the wing quarter-chord line), a second parameter study is carried out in terms of blade count effect. In this particular case, the results have shown that SRVs are capable of producing thrust of 12.2 counts at $N = 4$. However, besides thrust, negative lift is also generated by the vanes. To have constant total lift, the wing lift needs to be increased and consequently the induced drag. Taking this into account it is concluded that on constant lift, compared with the case without SRVs, the drag of the system has decreased by 6.1 counts, which is equivalent to 2.4% of propeller thrust.

References

[1] European Commission, "Annual Analyses of the EU Air Transport Market 2016," https://ec.europa.eu/transport/sites/transport/files/2016_eu_air_transport_industry_analyses_report.pdf.

[2] International Civil Aviation Organization, "ICAO Environmental Report 2016," http://www.icao.int/environmental-protection/Documents/ICAO%20Environmental%20Report%202016.pdf.

[3] International Air Transport Association, "Future of the Airline Industry 2035," https://www.iata.org/policy/Documents/iata-future-airline-industry.pdf.

[4] Lombardi, L., "ATR, Program Review and Market Outlook," *10th EWADE Conference*, Council of European Aerospace Societies, Naples, May 2011.

[5] ATR, "Connecting the Future, Turboprop Market Forecast 2018–2037," http://www.atraircraft.com/datas/download_center/151/1011_makretforecast_digital_151.pdf.

[6] Bombardier Aerospace, "Market Forecast 2017–2036," https://ir.bombardier.com/var/data/gallery/document/01/87/55/05/15/BCA-2017-2036-Market-Forecast-EN.pdf.

[7] ATR Marketing Department, "Regional Market Outlook, Turboprop Perspective 2010–2029," http://www.atraircraft.com/media/downloads/Regional%20Market%20Outlook%202010-2029.pdf.

[8] Beck, N., Radespiel, R., Lenfers, C., Friedrichs, J., and Rezaeian, A., "Aerodynamic Effects of Propeller Slipstream on a Wing with Circulation Control," *Journal of Aircraft*, Vol. 52, No. 5, 2015, pp. 1422–1436. doi:10.2514/1.C032901

[9] Kroo, I., "Propeller-Wing Integration for Minimum Induced Loss," *Journal of Aircraft*, Vol. 23, No. 7, 1986, pp. 561–565. doi:10.2514/3.45344

[10] Miranda, L., and Brennan, J., "Aerodynamic Effects of Wingtip-Mounted Propellers and Turbines," *4th Applied Aerodynamics Conference*, AIAA Paper 1986-1802, June 1986. doi:10.2514/6.1986-1802

[11] Witkowski, D. P., Lee, A. K., and Sullivan, J. P., "Aerodynamic Interaction Between Propellers and Wings," *Journal of Aircraft*, Vol. 26, No. 9, 1989, pp. 829–836. doi:10.2514/3.45848

[12] Veldhuis, L. L. M., "Propeller Wing Aerodynamic Interference," Ph.D. Dissertation, Dept. of Aerospace Engineering, Delft Univ. of Technology, Delft, The Netherlands, 2005.

[13] Miller, C. J., "Euler Analysis of a Swirl Recovery Vane Design for Use with an Advanced Single-Rotation Propfan," *AIAA/SAE/ASME/ASEE 24th Joint Propulsion Conference*, AIAA Paper 1988-3152, July 1988. doi:10.2514/6.1988-3152

[14] Dittmar, J. H., and Hall, D. G., "The Effect of Swirl Recovery Vanes on the Cruise Noise of an Advanced Propeller," *13th Aeroacoustics Conference*, AIAA Paper 1990-3932, Oct. 1990. doi:10.2514/6.1990-3932

[15] Gazzaniga, J. A., and Rose, G. E., "Wind Tunnel Performance Results of Swirl Recovery Vanes as Tested with an Advanced High Speed Propeller," *AIAA/SAE/ASME/ASEE 28th Joint Propulsion Conference and Exhibit*, AIAA Paper 1992-3770, July 1992. doi:10.2514/6.1992-3770

[16] Wang, Y., Li, Q., Eitelberg, G., Veldhuis, L. L. M., and Kotsonis, M., "Design and Numerical Investigation of Swirl Recovery Vanes for the Fokker 29 Propeller," *Chinese Journal of Aeronautics*, Vol. 27, No. 5,

2014, pp. 1128–1136.
doi:10.1016/j.cja.2014.03.009

[17] Stokkermans, T. C. A., Van Arnhem, N., and Veldhuis, L. L. M., "Mitigation of Propeller Kinetic Energy Losses with Boundary Layer Ingestion and Swirl Recovery Vanes," *Royal Aeronautical Society Applied Aerodynamics Conference*, Royal Aeronautical Soc., London, 2016.

[18] Li, Q., Öztürk, K., Sinnige, T., Ragni, D., Eitelberg, G., Veldhuis, L. L. M., and Wang, Y., "Design and Experimental Validation of Swirl Recovery Vanes for Propeller Propulsion Systems," *AIAA Journal*, Vol. 56, No. 12, 2018, pp. 4719–4729.
doi:10.2514/1.J057113

[19] Stokkermans, T. C. A., "Design and Analysis of Swirl Recovery Vanes for an Isolated and a Wing Mounted Tractor Propeller," M.Sc. Thesis, Dept. of Aerospace Engineering, Delft Univ. of Technology, Delft, The Netherlands, 2015.

[20] Ortun, B., Boisard, R., and Gonzalez-Martino, I., "In-Plane Airloads of a Propeller with Inflow Angle: Prediction vs. Experiment," *30th AIAA Applied Aerodynamics Conference*, AIAA Paper 2012-2778, June 2012.
doi:10.2514/6.2012-2778

[21] ATR, "ATR Family," http://www.atraircraft.com/products_app/media/pdf/FAMILY_septembre2014.pdf.

[22] Van Dam, C. P., and Nikfetrat, K., "Accurate Prediction of Drag Using Euler Methods," *Journal of Aircraft*, Vol. 29, No. 3, 1992, pp. 516–519.
doi:10.2514/3.46194

[23] Yamazaki, W., Matsushima, K., and Nakahashi, K., "Drag Decomposition-Based Adaptive Mesh Refinement," *Journal of Aircraft*, Vol. 44, No. 6, 2007, pp. 1896–1905.
doi:10.2514/1.31064

[24] Blackwell, J., "Numerical Method to Calculate the Induced Drag or Optimal Span Loading for Arbitrary Non-Planar Aircraft," NASA SP-405, May 1976.

[25] Lotstedt, P., "Accuracy of a Propeller Model in Inviscid Flow," *Journal of Aircraft*, Vol. 32, No. 6, 1995, pp. 1312–1321.
doi:10.2514/3.46880

[26] Jones, D. R., Perttunen, C. D., and Stuckman, B. E., "Lipschitzian Optimization Without the Lipschitz Constant," *Journal of Optimization Theory and Applications*, Vol. 79, No. 1, 1993, pp. 157–181.
doi:10.1007/BF00941892

[27] Hansen, P., Jaumard, B., and Lu, S. H., "Global Optimization of Univariate Lipschitz Functions: I. Survey and Properties," *Mathematical Programming*, Vol. 55, Nos. 1–3, 1992, pp. 251–272.
doi:10.1007/BF01581202

[28] Bartholomew-Biggs, M. C., Parkhurst, S. C., and Wilson, S. P., "Using DIRECT to Solve an Aircraft Routing Problem," *Computational Optimization and Applications*, Vol. 21, No. 3, 2002, pp. 311–323.
doi:10.1023/A:1013729320435

[29] Watson, L. T., and Baker, C. A., "A Fully-Distributed Parallel Global Search Algorithm," *Engineering Computations*, Vol. 18, Nos. 1–2, 2001, pp. 155–169.
doi:10.1108/02644400110365851

[30] Cox, S. E., Haftka, R. T., Baker, C. A., Grossman, B., Mason, W. H., and Watson, L. T., "A Comparison of Global Optimization Methods for the Design of a High-Speed Civil Transport," *Journal of Global Optimization*, Vol. 21, No. 4, 2001, pp. 415–432.
doi:10.1023/A:1012782825166

P. G. Tucker
Associate Editor

This article has been cited by:

1. Tom C. A. Stokkermans, Leo L. M. Veldhuis. 2021. Propeller Performance at Large Angle of Attack Applicable to Compound Helicopters. *AIAA Journal* **59**:6, 2183-2199. [Abstract] [Full Text] [PDF] [PDF Plus] [Supplementary Material]